

Original Research

Performance of QRS Detection for Cardiac Magnetic Resonance Imaging With a Novel Vectorcardiographic Triggering Method

Jon M. Chia, MS,¹ Stefan E. Fischer, PhD,^{1,2} Samuel A. Wickline, MD,¹ and Christine H. Lorenz, PhD^{1*}

In many cardiac patients, image quality and/or scan efficiency is reduced due to imprecise R-wave ability to trigger the scan due to noise on the electrocardiogram (ECG) caused by the magnetic resonance (MR) environment. We developed a triggering system that uses the spatial information of the vectorcardiogram (VCG) to minimize the effects of MR-related noise on triggering. Fifteen volunteers underwent standard cardiovascular MR exams, and a total of 52,474 R-waves were evaluated with the algorithm, giving a performance index of 99.91%. The mean propagation delay of the system was -10.64 ± 3.19 msec, which falls within the real-time definition for cardiac MRI triggering. Five patients had arrhythmias consisting of premature ventricular depolarizations (PVDs) and supraventricular extra systoles. For those patients with PVDs, all arrhythmic beats were rejected unless they passed through the algorithm's reference point. The performance index for the arrhythmic patients approached 100%. VCG-based triggering has been demonstrated to provide near 100% triggering performance during cardiac MR examinations. *J. Magn. Reson. Imaging* 2000; 12:678–688. © 2000 Wiley-Liss, Inc.

Index terms: MRI; vectorcardiogram; magnetohydrodynamic effect; heart

AS THE NUMBER of cardiac and angiographic MR examinations increases, the use of triggered and gated scans will also increase. Since in cardiac MRI an image typically cannot be acquired in one heart cycle, the image acquisition has to be synchronized with the phasic motion of the heart. These scans rely on accurate detection of the R-wave of the electrocardiogram (ECG) to guarantee that each portion of an image is acquired at the same phase of the cardiac cycle. However, in many of these patients, image quality or scan efficiency

is reduced due to imprecise QRS detection. First, traditional noise sources that may disturb the ECG and cause faulty triggering include powerline interference, poor electrode contact, patient motion, muscle contraction, and ECG baseline drift or amplitude modulation due to respiration. Standard QRS detection algorithms that have been developed for general monitoring purposes work well with general ECG databases and healthy patients but may not suffice for MR due to additional sources of triggering artifacts caused by the MR environment. Furthermore, patient setup time can be long in practice due to the need for multiple trials of electrode placement to reduce MR environment-related noise before finding a suitable waveform for triggering.

A principal source of artifact in the ECG due to the magnetic field itself is the *magnetohydrodynamic effect*. This effect comprises a voltage induced by ions flowing within blood vessels that are exposed to the magnetic field, according to the Lorentz force (1–4). This voltage artifact is mainly superimposed on the ST segment on the ECG during the ejection of blood in systole. This flow artifact may exhibit a larger amplitude than the QRS complex in certain individuals, which can cause a false QRS detection in certain R-wave detection algorithms. This false trigger would then, in turn, compromise the temporal fiducial marker for the cardiac scan. Other sources of noise include that from the radiofrequency (RF) pulses (5,6) and the switching of the gradient fields (7,8). In all these cases, these signals induce a voltage in the patient-electrode setup that can compromise accurate detection of the R-wave when using the conventional QRS detection algorithms available in most scanners.

For a detection algorithm to be deemed robust in the MR environment, two issues must be addressed. First, with respect to the extraneous noise caused in the MR environment, the algorithm should not falsely detect the R-peak due to the additional noise. Second, real-time detection should be possible, which means that the processing of the algorithm should take less time than the recording of the ECG. An algorithm is also considered to be real-time if no element of “backward search” for the R-wave is required.

¹Center for Cardiovascular MR, Cardiovascular Division, Washington University Medical Center, St. Louis, Missouri.

²Philips Medical Systems, Best, The Netherlands.

Contract grant sponsors: the Barnes-Jewish Hospital Foundation, the Wolff Charitable Trust, Philips Medical Systems, and the Magnetic Resonance Equipment Corporation.

*Address reprint requests to: C.H.L., CMR Unit, Royal Brompton Hospital, Sydney Street, London SW3 6NP, United Kingdom.

E-mail: chlorenz00@aol.com

Received February 15, 2000; Accepted May 31, 2000.

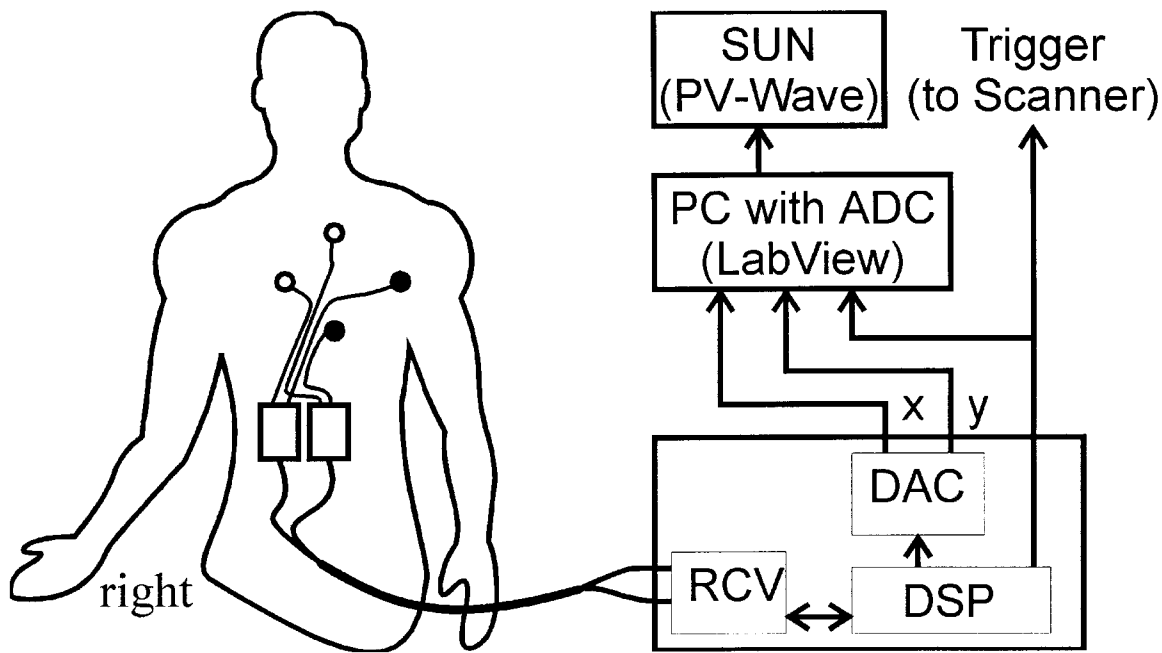


Figure 1. Diagram of data flow. RCV = fibreoptic receiver interface, DSP = digital signal processor, DAC = digital analog converter, ADC = analog to digital converter.

However, these two real-time requirements, while necessary, are not sufficient for the application of QRS detection algorithms in the case of triggered MR scans. The additional real-time requirement for ECG-triggered MRI is that the propagation delay, defined as the time between the R-peak and the generation of the trigger signal, should be less than 20 msec, for the reasons described below. In certain cardiac MR scans, ie, cine scans, a long propagation delay exists between the actual R-peak and when the detection of the R-peak could cause the end-diastolic image to be missed, since the time between the R-peak and the onset of mechanical systolic contraction ranges between 30 and 70 msec (9).

To overcome problems of extraneous noise while still detecting and triggering in real time, we have proposed that the use of the spatial information in a vectorcardiogram (VCG) can likely improve the R-wave detection in the MR environment (10). In a vectorcardiograph system, a three-dimensional (3D) orthogonal lead system is used, such as the Frank lead system, which registers dipole-resolved cardiac electromotive forces over the heart cycle. During cardiac depolarization, the resultant dipolar cardiac electromotive forces can be displayed as a "spatial vector" that varies in magnitude and direction throughout the cardiac cycle. Thus, a 3D path can be traced in time and space through the cardiac cycle by the VCG. Fortunately, it has been shown previously that the average electrical moment of the heart and the average moment of the flow artifact manifest significantly different spatial orientations (11). A separation of the QRS loop and the blood flow-induced artifact is also manifested in a 2D projection of the 3D VCG (11). Through judicious use of both temporal and spatial information, cardiac triggering can be arranged to avoid the flow artifact with the use of VCG, compared with triggering from 1D, or scalar, ECG. The purpose of

this study was therefore to evaluate the performance of a novel 2D VCG triggering system (11) for scan triggering during standard cardiac MR exams.

MATERIALS AND METHODS

VCG Triggering System

A prototype VCG triggering system was developed that utilizes the ECG signals from electrodes placed in a "cross" arrangement on the thorax (shown in Fig. 1) and converts them into planar VCG signals (11). Using this spatial information, the QRS complex is detected and a trigger signal generated. This trigger signal is sent to the MR scanner to synchronize the scans while the output electrical signals are simultaneously digitized and stored on an offline computer. The lead placement and the overall signal flow are shown in Fig. 1. Note that the reference ground electrode is not shown.

VCG QRS Detection Algorithm

The algorithm implemented in the prototype VCG triggering system uses a "target distance" approach (described below) to detect the R-peak (11). The VCG triggering system consists of two steps: the preparation phase and the real time QRS detection. Figure 2 shows the flow diagram of the VCG triggering algorithm. The preparation step establishes a reference point from which the algorithm monitors the spatial VCG in formation, as the spatial cardiac vector traverses a two dimensional x-y coordinate system, which inscribes a loop as it initiates and then returns to an isoelectric central point ("0 volts"). This path is referred to as a QRS loop. When the patient is outside of the magnet, the maximum amplitude of the loop as well as the maximum derivative of signal over time, determines the

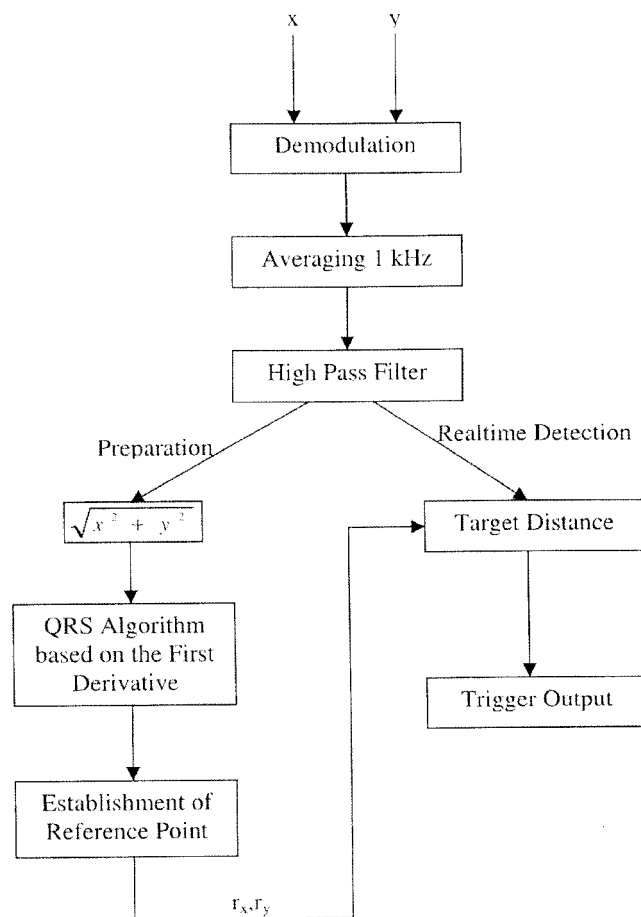


Figure 2. Target distance algorithm flow chart.

most likely region in space and time for the R-peak to occur. A reference vector, $r(t)$, is then derived, and a reference point is set as a threshold for triggering. After the reference point is determined, real-time detection of the QRS loop begins. During the real-time detection, the distance of the signal from each heartbeat, $s(t)$, is calculated against the reference vector. The probability of the heart signal being a QRS complex can be found using the calculated distance value and determination of where the vector passes through the established reference point. If the probability is higher than a set threshold, the signal is then determined to be a QRS. This is shown graphically in Fig. 3.

The trigger signal is transmitted to the MR scanner (Gyroscan ACS-NT PowerTrak 6000, Philips Medical Systems, Best, The Netherlands) to synchronize the MR acquisition. The output of the VCG system is comprised of the trigger signal and the derived orthogonal x and y leads from the 12-bit digital-to-analog outputs.

Subjects

A total of 15 volunteer subjects were studied. Twelve were males, and three were females, with an average age of 45 ± 16 years. Of the three women, two were healthy, and one had left bundle branch block (LBBB), with arrhythmic premature ventricular depolarizations (PVDs). Of the nine men, six were healthy, and three had a history of cardiovascular disease (mitral valve

prolapse and aortic insufficiency, hypertension, and coronary artery disease with an inferior myocardial infarction). In addition, four of the men had conduction defects and arrhythmias (three with left bundle branch block, LBBB, and PVDs; one with supraventricular extra systoles). A summary of the volunteers is shown in Table 1.

Before entering the MR scanner, all volunteers were screened to ensure safety, and all gave informed consent to the protocol approved by the local human studies committee. The area where the electrodes (ConMed, Utica, NY) were to be placed was first cleaned with alcoholic pads. The electrodes were then placed on the chest, as shown in Fig. 1, and connected to the FOX modules. The lead cables were twisted to reduce the small risk of thermal injury to the patient and to reduce extraneous gradient and RF noise. The FOX modules were then activated, and the VCG triggering program was started to obtain the reference point. After ensuring an acceptable reference, the electrode leads and FOX modules were taped to the subject to prevent motion artifacts. Then data collection commenced.

MR Imaging

All patients were scanned with the Gyroscan ACS-NT PowerTrak 6000 with a 1.5-T main magnetic field and gradient performance of 23 mT/m and 105 T/m/s.

For simplicity, the types of sequences applied in each volunteer are described as scan modules: ventricular function, real-time cine imaging, flow imaging, myocardial tagging, 3D coronary imaging, or carotid imaging. The ranges of scan parameters for these modules are outlined in Table 2. The particular scan modules that each volunteer underwent are described in Table 1.

The function module consisted of a series of prospectively triggered gradient-echo scans. Some of the gradient-echo scans used presaturation slabs for motion suppression. In addition, some subjects' spin-echo echoplanar scans also utilized a presaturation slab. All scans in the function module were performed using the body coil.

The tagging module consisted of an echoplanar imaging (EPI) sequence with additional RF prepulses to place a grid of nulled magnetization across the images (12). The real-time cine module consisted of a hybrid gradient-echo/EPI sequence. Both the tagging protocol and the real-time cine protocol used the synergy cardiac coil, which is a combination of a two-element phased array and a three-element quadrature coil to scan the region of interest (ROI). Flow imaging consisted of a retrospectively triggered gradient-echo sequence with flow-encoding gradients (phase-contrast MRI). The body coil was used to perform this scan.

The coronary imaging module consisted of gradient-echo scout images to isolate the ROI. Next, a prospectively triggered 3D gradient-echo sequence with navigator gating for motion suppression with a T2 preparation pulse to null the myocardium was performed.

The carotid imaging module consisted of a turbo spin-echo sequence and a 3D T1-weighted gradient-echo sequence. A 10-cm-diameter surface coil was used for both of these sequences.

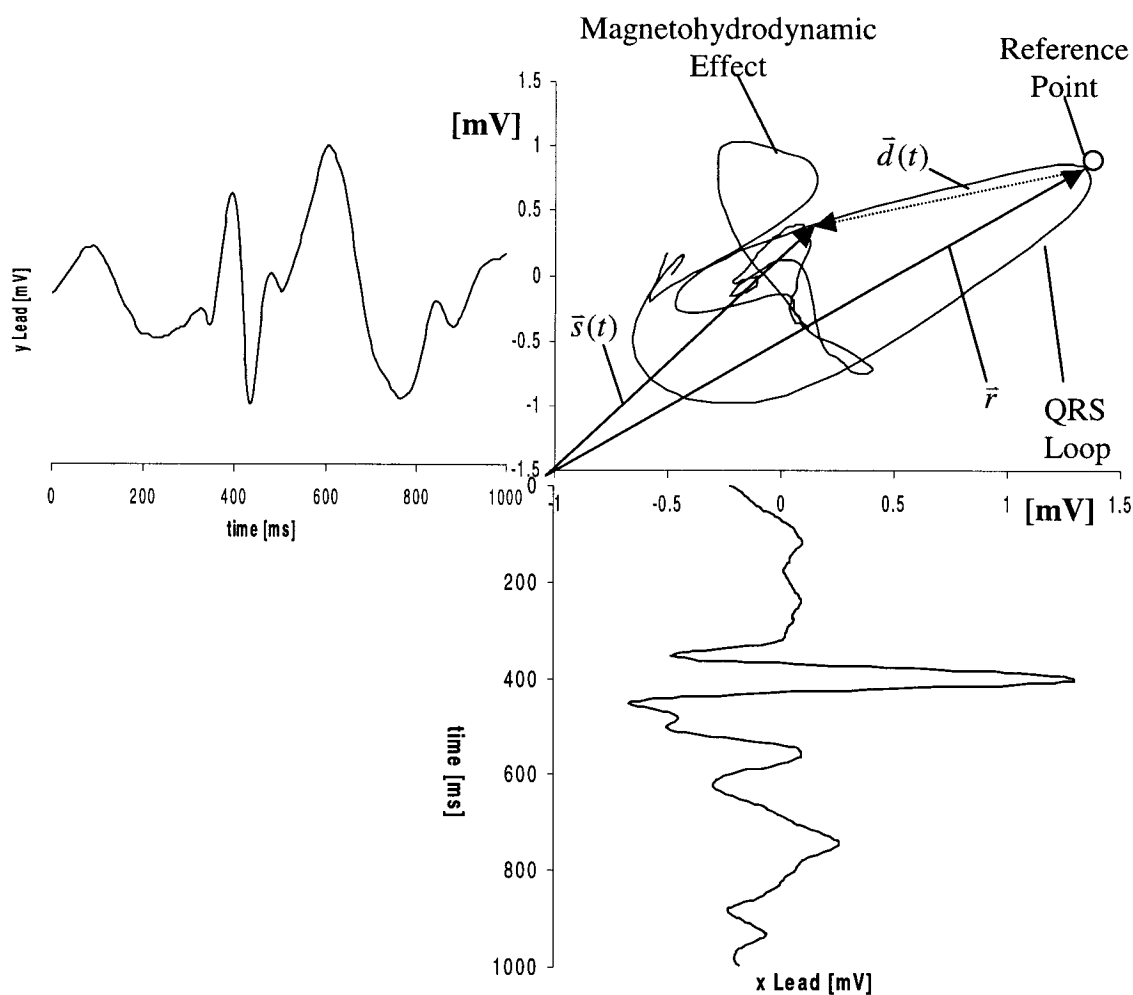


Figure 3. Graphical display of the target distance algorithm.

VCG Data Collection

The VCG and trigger signals are passed to a PC with a 100-MHz processor, 32 MB of RAM, 256 k of cache memory running Windows 95 (Microsoft, Redmond, WA) connected to the AT-MIO-16DE-10 data acquisi-

tion board (ADC), where they are viewed and saved with LabVIEW (version 5.01) Graphical Programming for Instrumentation (National Instruments, Austin, TX). Data were acquired at two rates: high resolution at a 1-kHz sampling rate and low resolution at 50 Hz.

Table 1
Volunteer Scan Protocols*

ID no.	Gender	Status	Scans
1	M	Healthy	Function, real-time
2	M	Hypertension	3D coronary-T2 preparation
3	M	Healthy	Function, flow, tagging
4	M	MVP, AI	Function, flow, tagging, real-time
5	F	Healthy	Function, flow, tagging, real-time
6	F	Healthy	Function, flow
7	M	Healthy	Function
8	M	Healthy	Function
9	M	Healthy	Function
10	M	Healthy	Function
11	M	LBBB, PVD	Function, perfusion
12	M	LBBB, PVD, CAD, MI	Function, carotid, perfusion
13	F	PVD	Function
14	M	SVES	Function, perfusion
15	M	LBBB, PVD	Function, perfusion

*LBBB = 3, AI = 1, PVD = 4, SVES = 1.

Table 2
General Scan Module Parameter Ranges*

FOV (mm)	Slices/phases	RFOV %	Scan %	No. of shots	TE/TR/FL (msec/msec/deg)	EPI factor
90–450	1–14/16–40	65–100	45–75	1–13	2–21/4–857/15–90	3–7

*The scans included are spin-echo EPI, segmented gradient-echo cine, CSPAMM, real-time cine, phase contrast flow, 3D T2 prep, T2 turbo-spin echo, and 3D T1 gradient-echo.

Field of view (FOV) = linear dimension selected to accommodate the anatomic region of interest.

Rectangular field of view (RFOV) = spacing between k-lines is enlarged, but k-space size remains the same.

Scan percentage = only a certain percentage of k-space is acquired; the unacquired lines are zero-filled.

Half scan = asymmetric fraction of k-space is acquired, and then the rest of k-space is copied.

Number of shots = the number of phase-encoding steps in one heart cycle.

Echo time (TE) = time between the RF pulse and the maximum amplitude of the first echo signal.

Repetition time (TR) = time between two subsequent excitations.

Flip angle (FL) = angle of rotation due to the RF pulse.

EPI factor = number of phase-encoding steps acquired in one heart cycle for EPI.

The high-resolution data were used to determine propagation delay and also to view the VCG. To determine the propagation delay between the trigger signal and the R-wave of the QRS complex, a 20-second segment of data was recorded at a sampling rate of 1 kHz. Three analog channels were recorded. Two of the channels recorded the two orthogonal leads, while the third channel recorded the resulting real-time trigger signal. During this time, 20-second segments were displayed at each time frame, and each 20-second segment was stored in memory.

The low-resolution data were used to determine the accuracy of the triggering algorithm during MR scanning. The saved data were processed on a Sparcstation 20 (Sun Microsystems, Mountain View, CA) with PV-Wave Advantage (Visual Numerics, Houston, TX). Custom PV-Wave routines were developed to quantify the saved data as well as the determination of average propagation delay.

Algorithm Evaluation

To determine the effectiveness of the algorithm, the sensitivity, specificity, and performance index were computed. This was also performed in a customized PV-Wave program. The data were visually displayed on the screen in 20-second segments. Using a mouse click, a hypothetical trigger point could be manually inserted by the user at the approximate location of each R-peak. The R-peak was then determined by calculating the maximum magnitude of the two lead signals within a 50-msec window of where the mouse pointer was clicked. Each trigger was then saved.

After all the R-waves in the entire data set were identified, the number of R-peaks, the number of false negatives, and the number of false positives were calculated compared with the trigger points determined by the algorithm. To determine the total number of R peaks (N), the manually inserted triggers were counted for the entire file. To determine the number of false negatives (FN), a 100-msec window was searched from where a manually inserted trigger was detected. If no VCG-generated trigger was found within that window, it was assumed that a trigger was missed. The number of false positives (FP) was determined by searching a 100-msec window from where a VCG trigger was located. If a manually inserted trigger was not found within this

100-msec window, then it was assumed that a false positive had occurred.

From these values, the sensitivity, specificity, and performance index (13) could be determined. The equations for calculating sensitivity and specificity are shown in Eqs. [1] and [2], respectively. The equation for performance index is shown below in Eq. [3], where N = total number of R-peaks, FP = number of false positives, FN = number of false negatives, and PI = performance index (14):

$$\text{Sensitivity} = \frac{N - FN}{N} \quad (1)$$

$$\text{Specificity} = \frac{N - FP}{N} \quad (2)$$

$$PI = \frac{[N - (FN + FP)]}{N} \quad (3)$$

These definitions of sensitivity and specificity differ slightly from conventional definitions (15) but accord with definitions used in previous studies on QRS detection algorithm performance (14).

In addition to the accuracy of the VCG-based QRS detection, the trigger timing stability was evaluated using the data sets recorded at a sampling rate of 1 kHz. The absolute local maximum of the VCG amplitude derived from the x and y channel in the frontal plane was identified and marked as the R-peak. The propagation delay was defined as the time interval between the R-peak marker and the onset of the trigger signal from the QRS detection algorithm. Thus, this time interval includes the filter delays of the FOX modules, the digital filter group delays, and the effective propagation delay of the QRS detection algorithm. A negative propagation delay means that a QRS complex is detected before the R-peak. For each individual patient, the propagation delay of each individual QRS complex within the 20-second recording was averaged, and the standard deviation was denoted as jitter. A large jitter would indicate a low timing accuracy of the detection algorithm, yielding blurring of the cardiac MR images. Furthermore, the average of the individual propagation

Table 3
Summary of Propagation Delay Values

ID no.	Propagation delay (msec)					
	Mean	Jitter	QRS (no.)	Min	Max	DIFF
1	-10.07	1.3	28	-12	-7	5
2	-8.88	1.26	24	-11	-7	4
3	-8.75	0.64	20	-10	-8	2
4	-7.74	0.71	34	-9	-6	3
5	-14.68	1.43	22	-17	-12	5
6	-9.8	0.76	30	-11	-8	3
7	-10.24	0.83	25	-12	-9	3
8	-14.14	1.42	21	-16	-11	5
9	-7.71	2.74	24	-12	-1	11
10	-13.6	1.39	20	-15	-11	4
11	-10.28	0.79	25	-12	-9	3
12	-11.84	0.92	38	-13	-10	3
13	-18.26	2.26	38	-25	-15	10
14	-6.55	0.83	20	-8	-5	3
15	-8.71	0.99	14	-10	-7	3
Average	-10.64	1.18		-12.5	-8.25	4.25
SD	3.19	0.59		4.17	3.29	
Total			363			

delays is the value that should be used to calculate the effective trigger delay of the MR sequence, the time between the R-peak, and the acquisition of the MR echo. The standard deviation of the individual propagation delays is an indicator for the predictability of the trigger time point.

RESULTS

In 14 of the 15 patients, the initial electrode placements sufficed to achieve an acceptable reference point for triggering. In one patient (volunteer 12), due to the initial low amplitude of the ECG, the electrodes had to be placed further apart. Only the data set from this second iteration of electrode placement was included in the study.

Table 3 summarizes the timing results of all subjects. A total of 363 heart beats were evaluated. The average propagation delay was -10.6 ± 3.2 msec, which means that the QRS complex was detected prior to the R-peak and that the trigger can be predicted within an interval shorter than 7 msec. The average jitter was 1.2 ± 0.6 msec, whereas all the trigger points were found in an interval from -25 msec to -5 msec with respect to the R-peak.

Figure 4 shows the output signals from the VCG system of a healthy volunteer. In this figure the magnetohydrodynamic artifact is very prominent in the y direction. Figure 5 shows the frontal loop (x-y plane) of the same volunteer. In this figure the magnetohydrodynamic artifact is clearly seen to be in a different orientation than the QRS loop. In this individual the angle

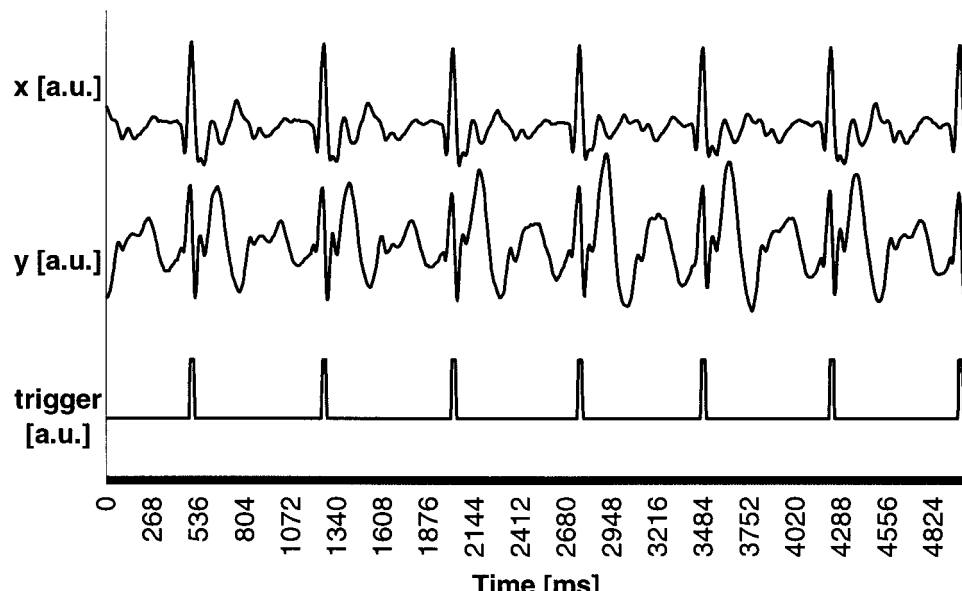


Figure 4. Sample output signals from a volunteer.

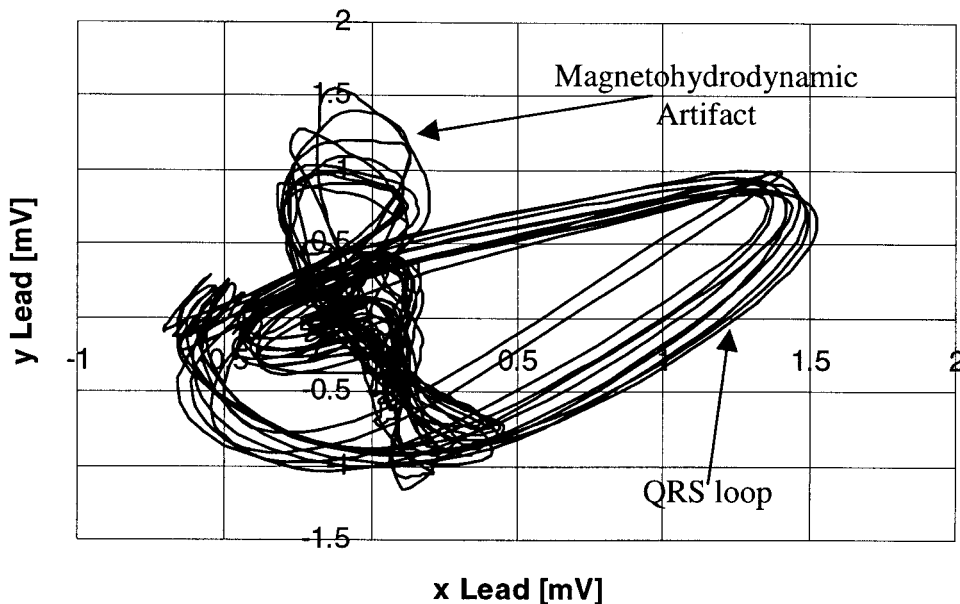


Figure 5. Frontal VCG loop from a volunteer.

between the magnetohydrodynamic artifact and the QRS loop is 62°.

Table 4 shows the individual performance of the algorithm for each volunteer and the overall performance of the algorithm of all volunteers. As noted, the total performance index of the VCG triggering system approaches 100%. In addition, the total performance index for each individual approaches 100%.

Table 5 shows the statistics of the VCG system for healthy and nonhealthy individuals without arrhythmias and/or conduction defects. The performance indices of the healthy volunteers and nonhealthy volunteers were equivalent. One of the nonhealthy volunteers had mitral valve prolapse and aortic insufficiency. The

other nonhealthy volunteer had hypertension. Neither of these two volunteers had conduction defects or arrhythmias. Hence, there were no changes in the shape or orientation of the QRS loop, compared with normal patients, resulting in expected robust performance of the VCG system. From Table 5 it can be seen that the performance index of both groups approached 100%. Across all subjects, 25 false positives were due to sudden movements of the chest, ie, coughing or arm movement. These movements superimposed noise onto the VCG that passed through the reference point and triggered the scan.

Figure 6 shows sample output signals from the VCG system of a patient with PVDs. The VCG algorithm can

Table 4
Summary of Results

ID no.	No. of R peaks	False positives	False negatives	Sensitivity (%)	Specificity (%)	Performance index (%)
1	4374	2	1	99.98	99.95	99.93
2	4384	3	0	100.00	99.93	99.93
3	5089	2	1	99.98	99.96	99.94
4	4615	8	2	99.96	99.83	99.78
5	3744	0	0	100.00	100.00	100.00
6	3239	2	1	99.97	99.94	99.91
7	2544	2	1	99.96	99.92	99.88
8	2286	0	0	100.00	100.00	100.00
9	3036	1	1	99.97	99.97	99.34
10	2854	5	1	99.97	99.82	99.79
11	3290	4	0	100.00	99.86	99.86
12	2824	4	0	100.00	99.85	99.85
13	4949	3	1	99.98	99.94	99.93
14	2544	0	0	100.00	100.00	100.00
15	2702	1	0	100.00	99.98	99.98
Total	52474	37	9	99.93	99.98	99.91
Healthy	26702	21	6	99.98	99.92	99.90
Diseased	25772	16	3	99.99	99.94	99.93
Female	12803	13	4	99.97	99.90	99.87
Male	39671	24	5	99.99	99.94	99.93

Table 5
Summary of Results for Nonarrhythmic Patients (Subjects 1–10)

ID	No. of R peaks	False positives	False negatives	Sensitivity (%)	Specificity (%)	Performance index (%)
Total	36165	25	8	99.98	99.93	99.91
Healthy	26702	21	6	99.98	99.92	99.90
Diseased	9463	4	2	99.98	99.96	99.94
Female	7854	10	3	99.96	99.87	99.83
Male	28311	15	5	99.98	99.95	99.93

distinguish the difference between a PVD and a normal QRS complex. Examination of the conventional ECG signals reveals that the PVD can manifest only slight differences from normal QRS complex in scalar leads. The differences are apparent in the timing and the amplitude of the PVD. Here, it can be seen that the PVD occurs more closely in time after a normal QRS complex and thus would be rejected by standard algorithms only if the R-R window is set large enough to exclude it.

Figure 7 shows the frontal VCG plot from a volunteer. Here it can clearly be seen that the PVD has a different shape than the QRS loop. In addition, the PVD is in a different orientation, so it does not pass through the reference point. Thus, the VCG target-distance algorithm does not mistake the PVD for a normal QRS loop. This difference in VCG characteristics between the normal and premature beats was first shown in a study performed by Talbot et al. In this study, they found that extrasystolic QRS loops differ in shape as well as orientation from normal QRS loops (16).

Table 6 shows the summary of results for the five volunteers with conduction defects and/or arrhythmias. In three of these volunteers, all arrhythmic QRS complexes were rejected. In all cases, the arrhythmias were PVDs in which the arrhythmia loop was in a different orientation than the normal QRS loop. In volunteer 14, no arrhythmias were rejected. This volunteer had supraventricular extra systoles. In this type of arrhythmia, the arrhythmic loop is the same shape and orientation as the normal QRS loop. Hence, the algorithm triggers on the arrhythmic beats, which is appropriate since conduction and mechanical contraction through the ventricle are normal. The only distinguish-

ing feature between this arrhythmia and the normal QRS loop is the variation in the R-R duration. Volunteer 13 also had PVDs; however, not all the PVDs were rejected by the algorithm. In those beats not rejected, although the PVD loop was a different shape and orientation than the QRS loop, the loop still passed through the established reference point of the algorithm, resulting in a false trigger. Even though not all arrhythmic QRS complexes were rejected, the performance index of the VCG algorithm in this subject was 99.93%.

DISCUSSION

From this study it has been shown that the 2D VCG system yields a very high performance index, which should in turn improve image quality and reduce scan time. From our patient selection, the 2D method was successful in yielding a performance index approaching 100% in all patients. In no patient did the algorithm falsely trigger on the flow artifact. In addition, the triggering was unaffected by RF noise as well as gradient noise on the ECG. Also, the propagation delay is within the 20-msec threshold.

Comparison With other Triggering Algorithms

This algorithm has significant advantages over standard 1D ECG triggering algorithms that are currently used in cardiac MRI such as the amplitude, first derivative, and matching template algorithms.

The amplitude algorithm assumes that the R-peak has the highest magnitude in the ECG. The problem

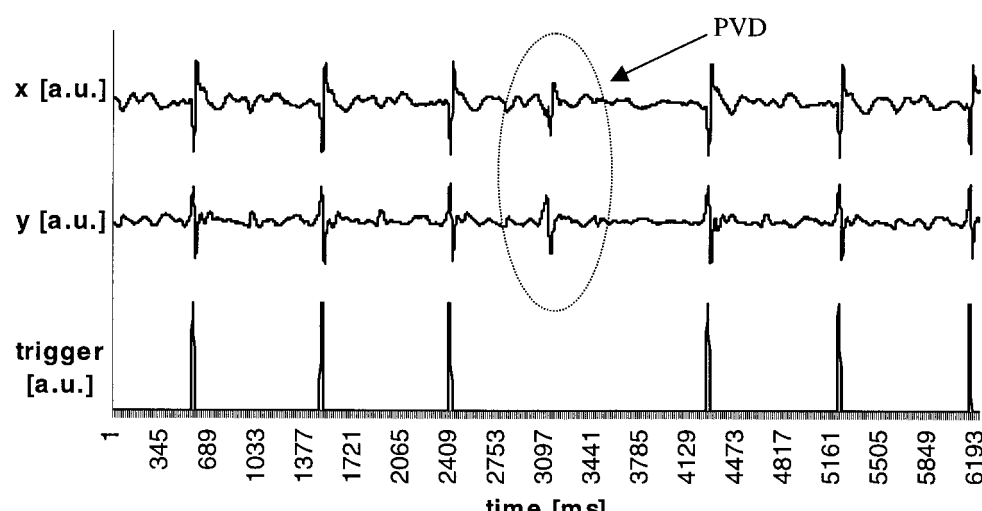


Figure 6. Sample output signals of a volunteer with PVDs.

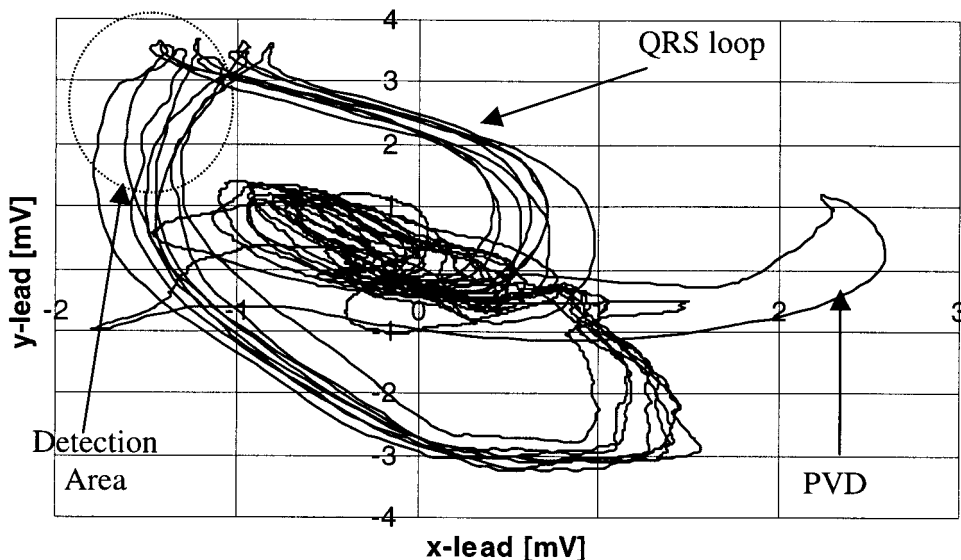


Figure 7. Frontal VCG loop from a volunteer with PVDs and LBBB.

with this algorithm is that sometimes the magnetohydrodynamic artifact has a larger amplitude than the R-peak. This algorithm may misinterpret the artifact as the R-peak; thus, a mistigger will occur. In addition, baseline drift causes the entire ECG to increase and decrease over time during the examination. If the baseline of the ECG is decreased below the determined threshold, the R-peak will not be detected. Thus, the MR scanner will fail to trigger accurately.

The algorithm based on the first derivative assumes that the QRS complex is the fastest rising component of the ECG (13). High-frequency noise, ie, that induced by switching gradient fields, may yield a first derivative higher than that of the QRS complex.

Matching template algorithms usually perform well if a representative QRS complex is identified. However, the propagation delay is greater than half of the QRS duration, which violates the real-time triggering criterion for cine acquisitions.

Arrhythmia Rejection

Current MR arrhythmia rejection methods compare each R-R interval retrospectively with a reference interval in order to accept or reject data associated with each trigger. This method fails in certain types of arrhythmias and is susceptible to failure due to heart rate variation, ie, during a cardiac stress test.

From our results, we have shown initial success in rejecting PVDs. With standard QRS detection algorithms, arrhythmic heartbeats can be mistaken as normal QRS complexes. This is undesirable for triggered cardiac MR examinations since image quality will be lowered when the R-R duration varies. However, rejecting only ectopic beats is not sufficient for improving image quality since the ventricular volume is different in the beats preceding and following the ectopic beat as well. In order to effectively perform arrhythmia rejection, one approach would be to combine the VCG triggering algorithm with current MR arrhythmia rejection algorithms based on R-R interval length. By combining these two methods, ectopic beats and their neighboring beats should be effectively rejected due to the extreme variation in the trigger intervals.

However, for a common arrhythmia such as atrial fibrillation, the R-R interval is highly variable, and an R-R interval-based algorithm succeeds in limiting the effects of R-R variation during a scan. Moreover, in atrial fibrillation there is no change in the shape of the QRS loop, so the VCG algorithm would not be able to reject these beats.

Future Work

One of the problems encountered by this algorithm is low VCG amplitude. Thus, the QRS loops in these pa-

Table 6
Summary of Results for Volunteers With Arrhythmias and Conduction Defects*

ID no.	Arrhythmic QRS				Normal QRS	
	Type	Rejected	Total	% Rejected	Total	PI
11	LBBB, PVD	38	38	100	3290	99.86
12	LBBB, PVD	8	8	100	2824	99.85
13	PVD	237	266	89	4949	99.93
14	SVES	0	213	0	2544	100
15	LBBB, PVD	206	206	100	2702	99.98

*SVES = supraventricular extrasystole.

tients will be smaller. Since the size of the detection area of the reference point remains the same size for all patients, these patients will be more susceptible to noise artifacts, ie, gradient noise and RF noise. Another problem with this algorithm is that it may give a false trigger due to sudden movements by the patient. This superimposes noise onto the VCG, which may pass through the reference point.

In women and excessively obese individuals, lead placement may have to be different since the breast or fatty chest may impede the standard lead placement. For these people an alternative lead placement may have to be found. One possibility could be to use the side of the body for the y and z leads. This will yield a "sagittal" VCG. Another possibility would be to place the leads farther apart. However, this might increase the noise from the MR. To determine a threshold for how far the electrodes can be apart, different electrode placements with varying distances and varying ground electrode placements must be tested.

However, in our initial experience with the 2D VCG setup, only one patient required a second iteration of electrode placement to achieve an acceptable reference point. This was due to the low signal-to-noise ratio of the initial ECG. Thus, if given an acceptable ECG signal, no trial and error electrode placement iterations are required to reduce MR environment noise and to achieve acceptable triggering performance. This will reduce the average patient setup time, which is an important requirement to introduce cardiac MR to wider clinical use. The independence of the lead setup and the reconstruction of the electrical axis of the heart also guarantee the predictability of the trigger time point with respect to the R-peak.

Improvement on the current algorithm in an attempt to eliminate the noise caused by sudden chest movement must still be implemented. The current algorithm has a very high sensitivity. However, to eliminate other noise sources, the specificity of the algorithm must be increased. Currently, with the target-distance reference point, the criteria that determine the likelihood of a QRS loop is the direction and whether or not the actual signal passes through the reference point. To increase the specificity, another reference point, r_2 , could be placed on the QRS loop half-way up the loop. This would add the shape of the loop as a criterion for acceptance. The equation with the addition of this criterion is shown in Eq. [4], where w is the weighting factor (ie, = 1) for the new criterion, $A_2(t)$ is the probability of the actual heart vector being a QRS signal (11), and Δt is the delay between the passing of reference point 2 with respect to the R-peak.

$$A_3(t) = A_2(t) \frac{w}{\max(|\rightarrow s(t - \Delta t) - \rightarrow r_2|, 0.01)} \quad (4)$$

The same extension could also be applied to arrhythmia rejection. Even though the orientation of the PVD arrhythmic loop has been shown to differ from the QRS loop, with regard to the target-distance algorithm, the arrhythmic loop could possibly still pass through the target-distance reference point, causing a false trigger.

Adding QRS loop shape criteria will increase the specificity of the algorithm, therefore enhancing the performance of the arrhythmia rejection.

Although the effect of accurate triggering on image quality was not evaluated in the present study, we have developed a simulation program (17) as a first step toward linking triggering accuracy and image quality. In this simulation k-lines are exchanged from different points in the cardiac cycle to mimic the effect of false triggers. One initial finding is that when there are more than 5% incorrect triggers during a scan, there is very noticeable blurring as well as signal-to-noise loss (17), highlighting the need for accurate triggering. However, to determine whether an image quality improves as a result of the use of this VCG triggering system, compared with a conventional triggering system, a clinical study will be required. For example, the same scan protocols could be run and compared for both triggering systems. This way quantifiable values such as ejection fraction, wall thickness, signal-to-noise ratio, and contrast-to-noise ratio can be compared between the two methods.

CONCLUSIONS

In this study the feasibility of VCG-triggered MR acquisitions has been demonstrated to result in high triggering performance. It has been shown that with the use of a VCG target-based algorithm, the performance index approaches 100%. In addition, the potential for robust rejection of PVDs, one of the most commonly seen arrhythmias, has been demonstrated. The combination of increased QRS detection accuracy, short propagation delay of the VCG system, and rejection of PVDs has the potential to increase the image quality as well as the scan efficiency. The standard lead placements used with the VCG system eliminate trial and error iterations for finding a suitable ECG waveform, thus reducing patient setup time. Reduction of setup time will improve throughput and therefore potentially improve the cost effectiveness of cardiac MRI. This triggering improvement should significantly impact on routine clinical cardiac MR image quality.

ACKNOWLEDGMENTS

The authors thank Kay Sayre, RN, MSN, for assistance with patient recruitment and Mary Watkins, RT(R) MR, for assistance with the MR scanning. The authors also thank Jan den Boef for helpful discussions.

REFERENCES

1. Togawa T, Okai O, Oshima M. Observation of blood flow EMF in externally applied strong magnetic field by surface electrodes. *Med Biol Eng* 1967;5:169-170.
2. Beischer DE, Knepton JC Jr. Influence of strong magnetic fields on the electrocardiogram of squirrel monkeys (*Saimiri sciureus*). *Aerospace Med* 1964;35:939-944.
3. Korchevskii EM, Marochnik LS. Magnetohydrodynamic version of movement of blood. *Biofizika* 1965;10:371-373.
4. Tendforde TS, Gaffey CT, Moyer BR, Budinger TF. Cardiovascular alterations in macaca monkeys exposed to stationary magnetic fields: experimental observations and theoretical analysis. *Bioelectromagnetics* 1983;4:1-9.

5. Damji AA, Snyder RE, Ellinger DC, Witkowski FX, Allen PS. RF interference suppression in a cardiac synchronization system operating in a high magnetic field NMR imaging system. *Magn Reson Med* 1988;6:637–640.
6. Shetty AN. Suppression of RF interference in cardiac gated MRI, a simple design. *Magn Reson Med* 1988;8:84–88.
7. Polson MJR, Barker AT, Gardiner S. The effect of rapid rise-time magnetic fields on the ECG of the rat. *Clin. Phys Physiol Meas* 1982;3:231–234.
8. Rokeby R, Wendt R, Johnston D. Monitoring of acutely ill patients during nuclear magnetic resonance imaging, use of a time varying filter ECG gating device to reduce gradients artifacts. *Magn Reson Med* 1988;6:240–245.
9. Lentner C. Geigy Scientific tables: vol 5. Heart and circulation, 8th ed. West Caldwell, NJ: CIBA-GEIGY Corporation; 1990.
10. Frank E. An accurate, clinically practical system for spatial vectorcardiography. *Circulation* 1956;13:737–749.
11. Fischer SE, Wickline SA, Lorenz CH. A novel real-time R-wave detection algorithm based on the vectorcardiogram for accurate gated magnetic resonance acquisitions. *Magn Reson Med* 1999;42:361–370.
12. Fischer SE, McKinnon GC, Maier SE, Boesiger P. Improved myocardial tagging contrast. *Magn Reson Med* 1993;30:191–200.
13. Friesen GM, Jaqnett TC, Jadallah MA, et al. A comparison of the noise sensitivity of nine QRS detection algorithms. *IEEE Trans Biomed Eng* 1990;37:85.
14. Trahanias PE. An approach to QRS complex detection using mathematical morphology. *IEEE Trans Biomed Eng* 1993;40:201–205.
15. Shortliffe EH, Perreault LE. Medical informatics: computer applications in health care. Reading, MA: Addison-Wesley; 1990.
16. Talbot S, Kilpatrick D, Weeks B. Vectorcardiographic features of ventricular extrasystoles correlated with conventional scalar electrocardiographic interpretation. *Br Heart J* 1978;40:883–890.
17. Chia JM, Fischer SE, Wickline SA, Lorenz CH. Quantification of image quality due to poor triggering. *J Cardiovasc Magn Reson* 1999;1:349–350.